J. Fluid Mech. (2008), *vol.* 600, *pp.* 19–43. © 2008 Cambridge University Press
doi:10.1017/S0022112008000347 Printed in the United Kingdom

The origin of the tubular jet

RAYMOND BERGMANN, ERIK DE JONG,
JEAN-BAPTISTE CHOIMET, DEVARAJ VAN DER MEER
AND DETLEF LOHSE

Physics of Fluids Group, Department of Applied Physics, Impact Institute, and J.M. Burgers Centre for Fluid Dynamics, University of Twente, P.O. Box 217, 7500 AE Enschede, The Netherlands

(Received 2 February 2007 and in revised form 5 December 2007)

A vertical cylindrical tube is partially immersed in a water-filled container and pressurized to lower the fluid level inside the tube. A sudden release of the pressure in the tube creates a singularity on top of the rising free surface. At the very beginning of the process a jet emerges at the centre of the surface, the strength of which strongly depends on the initial shape of the meniscus. Here, the time-evolution of the complex shape of the free surface and the flow around the cylindrical tube are analysed using high-speed imaging, particle image velocimetry, and numerical simulations. The tubular jet is found to be created by the following series of events, which eventually lead to the flow focusing at the tube's centre. A circular surface wave, produced by the funnelling of flow into the tube, is pushed inwards by the radial flow directly underneath the surface. As the wave moves inward and eventually collapses at the centre of the tube, a bump of fluid grows in the centre due to the converging flow in the bulk. This converging flow continues to feed the jet after the circular wave has collapsed. The singularity of the wave collapse is manifested in the initial sharp tip of the jet. All of the above events are traced back to a single origin: the convergence of the flow as it enters the tube. Movies are available with the online version of the paper.

1. Introduction

Liquid jets emerge when a relatively large amount of kinetic energy is imparted to a small mass of liquid near a free surface. In this paper we will concentrate on the mechanism that produces the particularly intriguing 'tubular jet'.

The tubular jet can be observed in a simple experiment in which a liquid rushes upwards to fill an initially pressurized, vertical tube partially immersed in a bath of fluid (see figure 1). As the liquid begins to rise in the tube after the pressure release, in some cases a jet can be seen to emerge from the centre of the surface of the rising liquid column. Figure 2(*b*) shows a typical example of such an experiment. This tubular jet was first reported by Lorenceau *et al.* (2002), in a paper that mainly focused on the oscillating motion of the liquid column as a whole. Although the authors discussed some of the jet's properties, it remained unclear what the driving and focusing mechanisms for this jet are.

Mechanisms to focus momentum into a liquid jet are known to occur in great variety. Examples are the jet produced by the printhead of an inkjet printer, where a pressure wave in an open-ended channel is focused on the free surface at the nozzle (Le 1998; Chen & Basaran 2002; de Jong *et al.* 2006*a*, *b*), or the jetting in a glass of champagne, where the surface tension stresses focus on the base of an unstable cavity

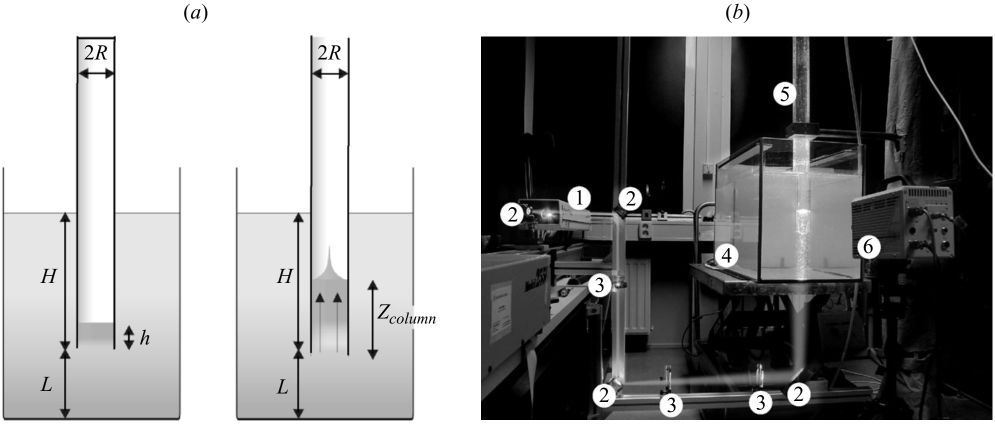

FIGURE 1. (*a*) Schematic drawing of the tubular jet setup, illustrating the main parameters of the experiment: R the inner radius of the tube, H the distance from the bottom of the tube to the water surface, L the distance from the bottom of the tube to the bottom of the tank, and h the initial water level in the tube. Left: initial situation; right: during the rise of the column. (*b*) The experimental setup in the laboratory with its main components labelled. 1: Argon-ion laser; 2: mirrors; 3: cylindrical lenses; 4: tank; 5: tube; 6: camera.

at the surface and are released in a liquid jet (Liger-Belair *et al.* 2001; Boulstone & Blake 1993). The jets produced by armour-piercing weapons have also been studied in detail (Birkhoff *et al.* 1948). In this case the focusing is found to be purely geometrical and the driving is provided by an explosive chemical reaction.

The jetting phenomena that are most closely related to the tubular jet are those created by what could be best described as a pressure-driven geometrical flow focusing. A first example is a tube filled with a perfectly wetting liquid falling axially under its own weight. On impact of the tube on a rigid floor, the sudden change in the tube velocity induces a pressure gradient which violently reverses the initial interface curvature, forming a concentrated jet (Antkowiak *et al.* 2007). A second example is the collapse of a surface cavity formed by the impact of a droplet or object onto a fluid surface. Such a cavity collapses under the influence of hydrostatic pressure and a pressure singularity occurs as the sides of the cavity collide, which is subsequently released by the formation of an upward and a downward jet (Worthington 1908; Longuet-Higgins, Kerman & Lunde 1991; Oguz & Prosperetti 1993; Blake *et al.* 1997; Gaudet 1998; Zeff *et al.* 2000; Zhang *et al.* 2001; Leppinen & Lister 2003; Suryo, Doshi & Basaran 2003; Burton, Waldrep & Taborek 2005; Gordillo *et al.* 2005; Bergmann *et al.* 2006; Eggers *et al.* 2007; Ducleaux *et al.* 2007). A similar void collapse is even observed in granular materials, when a steel ball impacts on a bed of very fine, loose sand (Thoroddsen & Shen 2001; Lohse *et al.* 2004; Royer *et al.* 2005; Caballero Robledo *et al.* 2007). After the ‘hydrostatic’ void collapse, a jet of sand shoots upward and another one downward.

In this paper we will show that the origin of the tubular jet is similar to the geometrical flow focusing examples discussed above, but with the considerable difference that the focusing geometry is now not provided by the topology of the free surface alone, but is in essence due to the tube wall partly obstructing the flow. Another distinct feature is that we find the tubular jet to reflect the interplay of several flow focusing events instead of a single mechanism as was the case in all the aforementioned jetting phenomena.

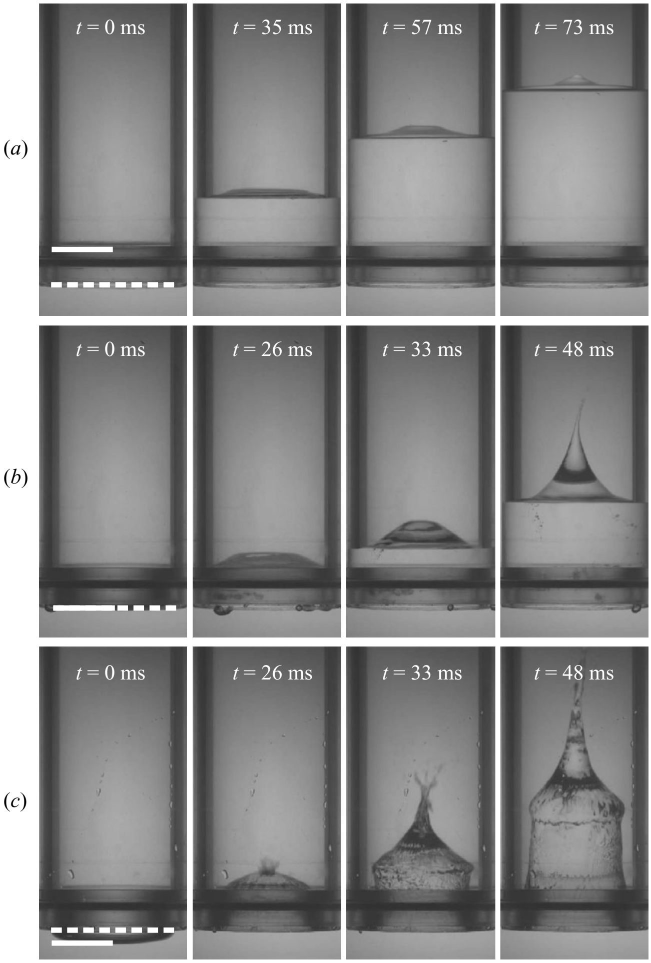

FIGURE 2. Different types of jets for (initial) meniscus heights $h = 14$ mm (*a*), $h = 0$ mm (*b*), and $h = -6$ mm (*c*) in a tube of inner radius $R = 25$ mm. The dotted white line indicates the bottom of the tube and the solid white line is the depth of the centre of the initial meniscus; $h > 0$ produces no jet, just a small bump of liquid in the centre of the tube, $h \approx 0$ produces a sharp jet, and $h < 0$ produces a detached rising water column from which a strong jet erupts. In all cases the distance L to the ground is much larger than R ($L \gg R$). The tube is submerged to a depth H of 200 mm. Available as movie 1 with the online version of the paper.

In § 2 we introduce the experiment and briefly discuss the relevant observations reported by Lorenceau *et al.* which serve as a starting point for the present investigation. Then in § 3 we discuss our own experimental setup together with the experimental considerations. After this, in § 4, we present results from particle image velocimetry experiments on the formation and closure of a surface cavity which precedes the jet eruption. In § 5 we investigate the role of radial flow on the jet eruption by comparing three different experimental configurations. To further support our interpretation of the results, numerical potential flow calculations of the jet formation are presented in § 6. In the concluding § 7 we summarize our findings.

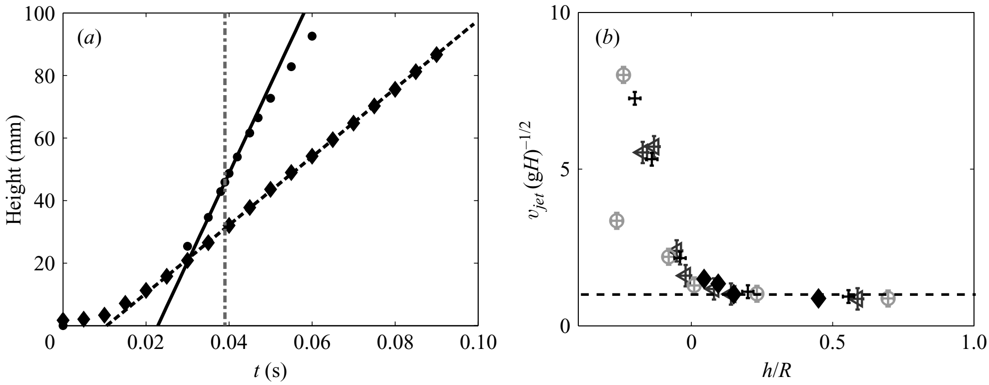

FIGURE 3. (*a*) The height of the water level in the tube z_{column} (diamonds) and the height of the jet (dots) as a function of the time since the release of the overpressure in the tube for $R = 25\,\text{mm}$, $L \gg R$, $H = 150\,\text{mm}$, and $h = 0\,\text{mm}$. The data are obtained by high-speed imaging at a 1000 frames per second. The vertical dot-dashed line indicates the moment of the jet eruption, when a sharp liquid spike becomes visible at the centre of the free surface in the tube. Since the jet height is defined as the height of the centre of the interface, it can exceed the column height before the actual moment of jet eruption owing to the rising rim. A linear fit is made to the column data (dashed line) after the jet eruption to obtain the column velocity v_{column} and a linear fit is made to the jet height (solid line) during the first 5 ms of the jet's existence to obtain the initial jet velocity v_{jet}. (*b*) The initial jet velocity v_{jet} non-dimensionalized by the velocity of the rising column $\sqrt{gH}$ as a function of the initial meniscus depth h normalized by the radius of the tube R. The black diamonds show the data obtained by Lorenceau *et al.* (2002) (for $R = 20\,\text{mm}$ and $H = 300\,\text{mm}$) and our experiments are shown by the data points with an error bar for the conditions of $R = 25\,\text{mm}$, $L \gg R$, and three values of H (dark grey triangles: $H = 150\,\text{mm}$, light grey circles: $H = 200\,\text{mm}$, black crosses: $H = 250\,\text{mm}$). It should be underlined that the tubular jet is not characterized by a constant velocity and that v_{jet} is the *initial* jet velocity which is obtained from the experimental data using the procedure described in (*a*). The dashed line indicates $v_{jet}/\sqrt{gH} = 1$.

2. Dynamics of a liquid column

When the overpressure inside a circular tube of inner radius R is released and suddenly drops to the ambient level in the tank, the water column rises freely from its initial level h to the (eventual) equilibrium level at H (both measured with respect to the bottom of the tube, see figure 1*a*). The initial height of the water column h is measured at the centre of the tube and the depth of immersion H is the distance from the bottom of the tube to the ambient water level. Lorenceau *et al.* (2002) derived expressions for the liquid column height $z_{column}(t)$ as a function of time by describing the rising liquid column in the tube as a (damped) oscillator with a continuously varying mass. For the initial rise in the time interval relevant for the development of the tubular jet ($t \ll 6\sqrt{H/g}$), $z_{column}(t)$ was found to be linear in time after a short period of initial acceleration (see figure 3*a*). The constant rise velocity of the column was found to be

$$v_{column} = \frac{\mathrm{d}z_{column}}{\mathrm{d}t} = \sqrt{gH}\,, \tag{2.1}$$

with g the gravitational acceleration. It is stressed that all derivations hold only for $H \gg R$ owing to the inclusion of entrance effects (dissipation by eddies).

As one starts with an initially empty tube, one would start with a singularity, as the mass of the liquid column $m_{column}(t) \propto z_{column}(t)$ is 0 at the start. This was recognized as

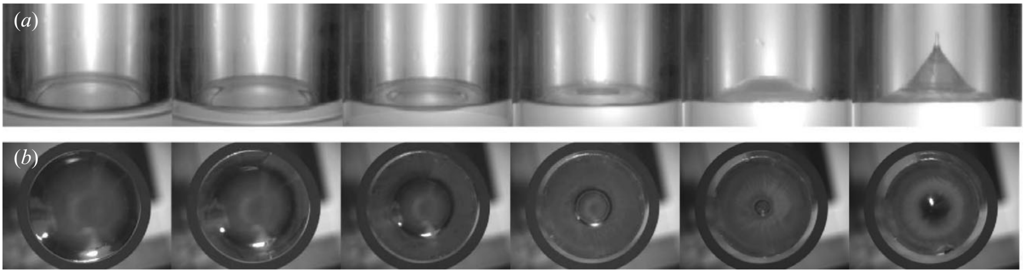

FIGURE 4. (*a*) Side view of the rim closure. (*b*) Rim closure seen from below (series similar to images in Lorenceau *et al.* 2002). The time between consecutive frames is 6 ms and for both series the experimental conditions are: $R = 25\,\text{mm}$, $L \gg R$, $H = 300\,\text{mm}$, and $h = 0\,\text{mm}$. Series (*b*) is available as movie 2 with the online version of the paper.

an unphysical feature of the model, since there is always a mass of liquid underneath the tube entrance that must be accelerated. An entrance length z_0 was defined as a measure of this added mass at the tube entrance, giving $m_{column}(t) \propto z_{column}(t) + z_0$, which was used to derive an equation to describe the initial acceleration stage of the rise

$$z_{column}(t) \approx h + \frac{gHt^2}{2(h + z_0)}, \tag{2.2}$$

valid for the first instants of the rise, when $t\sqrt{gH} \ll h + z_0$. The entrance length z_0 was found to be of the order of the inner radius of the tube R and not to depend on h.

It should be stressed that the above relations pertain only to the motion of the liquid column as a whole, and do not capture the motion of the jet itself. Lorenceau *et al.* did however make the following observations of the tubular jet. The maximum height reached was found to depend strongly on the initial level of the liquid in the column h. Note that h will have negative values for a meniscus bulging out of the tube and positive values when the air/liquid interface is located inside the tube. The tubular jet was found not to form at all for positive values of h, in this case only a small bump of liquid being observed at the interface, and for negative h a strong increase in the height of the jet was found as h decreased. It was also stated that the jet forms after a short, but significant, delay of order $t = R/\sqrt{gH}$.

Mention is made of the existence of a ‘liquid crater’ on the surface of the rising column. In figure 4 such a cavity can be clearly seen as a black ring due to the refraction of light through the curved shape of its rim. At the beginning of the rise, this circular cavity forms and closes onto itself. The propagation speed of the rim of this cavity was determined to be constant and the time needed to close the cavity was found to be equal to the time delay before jet eruption, when a sharp liquid spike becomes visible at the centre of the tube. This behaviour of the free surface is sketched in figure 5. When the tubular jet was absent, e.g. in the case of positive h, the rim was also not observed. The hypothesis of Lorenceau *et al.* (2002) was that the rim is related to a circular vortex which remains close to the entrance as the water flows into the tube. The objective of this paper is to check this hypothesis and, more generally, to shed light onto the formation and development of the jet.

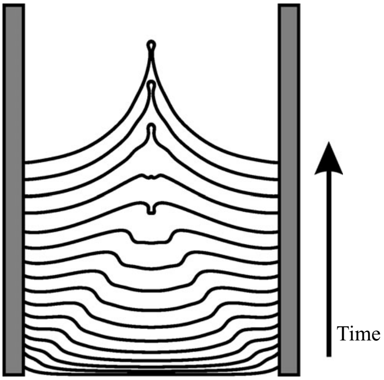

FIGURE 5. A sketch of the free surface in the tube at different times based on the observations of figure 4. Shortly after the pressure release a circular cavity forms and closes onto itself. The collapse of the circular wave coincides with the eruption of the tubular jet. Notice that due to the wetting properties of Perspex, the initial contact angle between the air/water interface and the inside of the tube is smaller than 90°.

3. Experiment

A schematic drawing and a picture of the setup we used for the investigation of the tubular jet can be found in figures 1(*a*) and 1(*b*), respectively. A vertical, cylindrical Perspex tube of inner radius $R = 25\,\mathrm{mm}$ is partially submerged to a depth H in a glass tank (dimensions 380 mm×780 mm×400 mm) which is filled to a depth $H + L$ with demineralized water. Since all experiments discussed in this paper were performed with H between 0.025 and 0.35 m, typical velocities for the rising water level are of the order of $\sqrt{gH} \approx 1\,\mathrm{m\,s^{-1}}$.

The top of the tube is connected to a compressed-air line in order to control the initial meniscus depth h by pressurizing the air inside the tube. The top of the tube is also connected to an electromagnetic valve which, when opened, causes the pressure inside the tube to instantly drop to the ambient level. The diameter of the outlet hose and valve opening is large enough such that the air flow is hardly restricted as it leaves the tube.

Outside the tank a high-speed camera is set up approximately level with the bottom of the tube, perpendicular to the glass sidewall of the tank. For the imaging of the experiment, a Kodak CR2000 CCD camera is used at a frame rate of 1000 frames per second and a resolution of 512×384 pixels. Backlighting of the tube is achieved by a halogen lamp with a diffusive plate placed at the opposite side of the tank to obtain typical images like those of figure 2.

The Reynolds number associated with the flow in the tube is

$$Re = \frac{2R\sqrt{gH}}{\nu}, \tag{3.1}$$

where ν is the kinematic viscosity of water. For the tube depths H of our experiments, the Reynolds number ranges between 2.5×10^4 and 9×10^4 and viscous effects can therefore be neglected for the main flow in the tube. Tube flow is generally turbulent for $Re > 4000$, so this system would be well within the turbulent domain. However, the flow is certainly not fully developed just as it enters the tube. For turbulent tube flow, the entrance length is given by (Munson, Young & Okiishi 1998)

$$l_e/2R = 4.4(Re)^{1/6}, \tag{3.2}$$

from which we calculate that for our case l_e is of the order of 1 m, which provides a typical time scale for the flow development of about 1 s. The turbulent flow suggested by the Reynolds number is clearly not yet developed on the time and length scales we are considering, namely those for the eruption of the tubular jet.

After the initial acceleration of the water column the Weber and Froude numbers associated with the tube flow are given by $We = \rho g H R/\sigma$ and $Fr = H/R$. Here ρ denotes the density of water and σ the surface tension at the interface. For our experiments the effect of surface tension can be neglected on the large scale of the tube, since the Weber number ranges between 9×10^2 and 1.2×10^4. The Froude number ranges between 1 and 14 which signals that the tube flow is indeed dominated by a balance of gravity and inertia. Surface tension does however have some influence on the shape of the meniscus, and thus affects the process of jet formation by changing the initial condition from which the experiment starts.

As discussed in § 2, we find that the initial depth of the centre of the gas/liquid interface h, in other words the meniscus, has a profound effect on the jet. Figure 3(*b*) shows the strong dependence of the initial jet velocity v_{jet} on h.

It should be underlined that the tubular jet is not characterized by a constant velocity; the initial jet velocity v_{jet} is measured through high-speed imaging in the first 5 ms after the jet erupts from the free surface (see figure 3*a*). For comparison the initial jet velocities obtained from figure 11 of Lorenceau *et al.* (2002) for a slightly smaller tube of $R = 20$ mm are also included in figure 3(*b*). Since figure 11 of Lorenceau *et al.* (2002) shows the time dependence of the jet height relative to the height of the water column, we can only compute the quantity $v_{jet} - v_{column}$ from this figure. To obtain the absolute value of v_{jet} we add v_{column} observed under the same conditions (although in a slightly larger tube) from our experiments to this result. Like the column velocity v_{column}, v_{jet} is found to scale with $\sqrt{gH}$, which facilitates the collapse of all velocity measurements for different H onto a single curve.

The influence of h can be classified into three different regimes:

(i) For an initial meniscus sufficiently far inside the tube ($h > 0$, figure 2*a*), the initial jet speed is of order $\sqrt{gH}$, in other words, $v_{jet} \approx v_{column}$. This corresponds to the horizontal asymptotic value of 1 in figure 3(*b*). There is no jet, only a bump on the water surface and the rim seen in figure 4 is also absent here.

(ii) For an initial meniscus flush with the bottom of the tube ($h \approx 0$, figure 2*b*), a rim is observed and a jet erupts shortly after the acceleration stage of the water column rise.

(iii) For an initial meniscus bulging sufficiently out of the tube ($h < 0$, figure 2*c*), the flow at the tube entrance cannot follow the 90° corner of the tube's inner edge, causing the rising column to separate from the inside wall of the tube. A very strong jet is formed at the top of this detached water column, contributing to the steep rise of the initial jet velocity in figure 3(*b*) for negative h. By rounding the edge of the tube the separation can be partly suppressed.

As the influence of h on the jet velocity has already been studied in Lorenceau *et al.* (2002), in the remainder of this paper we will focus on experiments with the initial meniscus being flush with the bottom of the tube ($h = 0$). In this case there is a clear tubular jet and we are unhindered by the possible separation of the liquid column from the inner wall of the tube as is common for $h < 0$. Looking at this regime will not limit the generality of our observations on the tubular jet, but will facilitate the comparison between the different flow configurations introduced in the later sections of this paper.

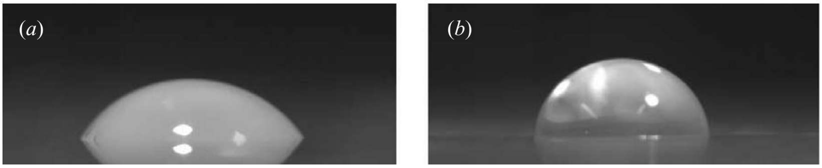

FIGURE 6. A droplet of water deposited on a clean and a vaseline covered Perspex surface. (*a*) The apparent contact angle of the air/water interface with Perspex is approximately 55°. (*b*) The apparent contact angle of the air/water interface with vaseline treated Perspex is about 85°.

4. Formation and closure of the rim

Although the rim of figure 4 is observed whenever the tubular jet forms and the jet eruption and rim closure are always simultaneous, it is not *a priori* clear that this rim is a prerequisite for jet eruption. To investigate this, we will try to unravel the origin and nature of this rim by answering the following questions:
Is the rim due to the initial capillary uprise of the meniscus detaching and travelling over the free surface?
Does the rim propagate like a capillary or gravitational surface wave?
Do entrance vortices cause the rim to form and propagate?

4.1. *Is the rim due to the initial capillary uprise of the meniscus detaching and travelling over the free surface?*

Owing to the wetting properties of Perspex, the initial air/water interface inside the tube curves up, when the distance to the inner wall is below the capillary length (see figure 6*a*). As the gas pressure inside the tube is released and the interface starts to accelerate upwards, this initial curvature of the interface could detach and travel over the surface as the rim.

To check whether the rim closure is indeed simply an inward propagation of the capillary uprise, we applied a small amount of vaseline to the tube entrance (cf. figure 6). This alters the contact angle between the interface and the tube, and will flatten the interface near the inner wall of the tube. However, using this hydrophobic tube entrance, the rim still formed and collapsed at the same constant velocity as was found for the regular case. The rim can therefore not be attributed to the detachment and propagation of the capillary uprise of the liquid at the wall.

4.2. *Does the rim propagate like a capillary or gravitational surface wave?*

The nature of the rim could reveal the mechanism by which it is produced. Therefore we made direct observations of the rim with a high-speed camera, to investigate whether it can be attributed to an initial disturbance which travels as a capillary or gravitational surface wave towards the axis of the tube.

Based on figure 4 it seems plausible that the wave is a capillary or gravitational surface wave, but in these recordings the camera was positioned horizontally and the fluid interface obscures largely what is happening at the centre of the fluid cavity. So, in order to make more revealing recordings, the high-speed camera was then mounted at an angle above the setup to allow us to view what happens inside the cavity as it collapses. The frames of figure 7 show these tilted recordings. The first striking observation from figure 7 is that the rim moves into a flat inner region of the interface with a steep front, more reminiscent of a hydraulic jump or bore than the smooth front expected for a surface wave. The second observation is that in the first two frames of figure 7 the rim, the size of which would correspond to a wavelength

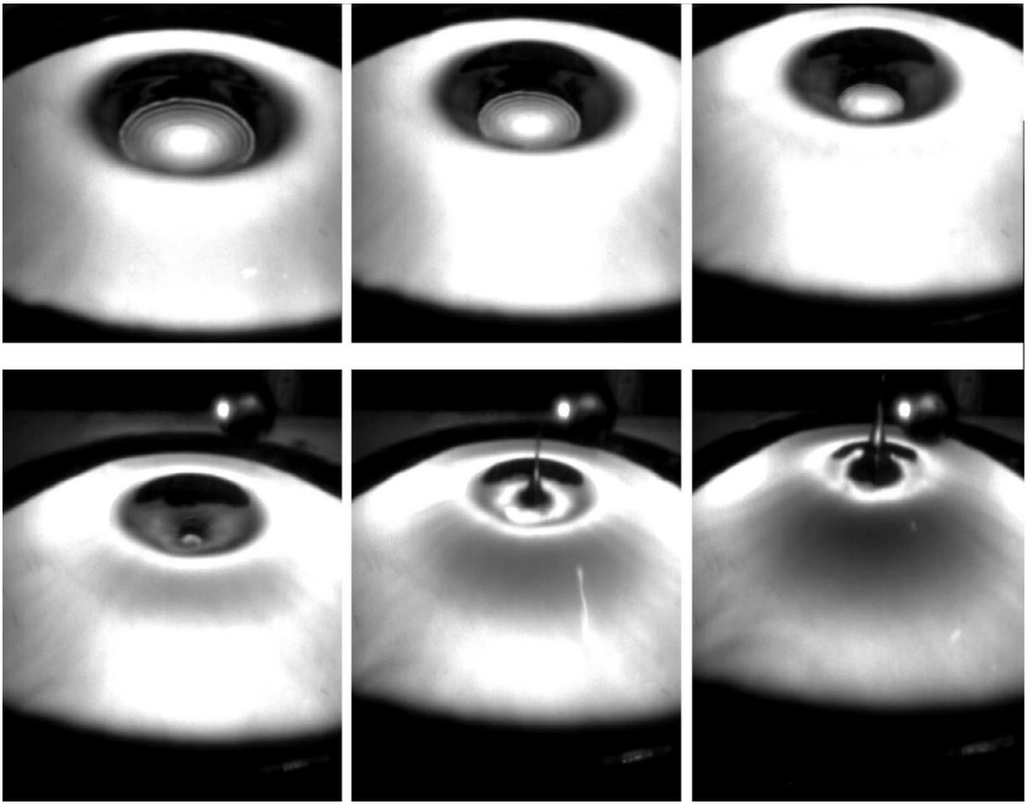

FIGURE 7. A series of images of the rim closure viewed from above at an angle for $R = 25$ mm, $L \gg R$, $H = 200$ mm, and $h = 0$ mm. The rim moves as a wall of fluid over the undisturbed inner region of the interface, much like a hydraulic jump (Bohr *et al.* 1993). The jet is initiated when the bottom of the fluid wall reaches the centre. The time between the images is 1 ms. Available as movie 3 with the online version of the paper.

of roughly 1 cm or larger, is preceded by small capillary waves with wavelengths λ smaller than 3 mm. These waves are observed from the start of the column rise, but are 'overtaken' by the rim in the third frame. This also rules out the wave being a capillary or gravitational wave, since these smaller capillary waves should propagate faster than a 1 cm gravitational wave (see Appendix A).

Based on these two observations of the shape and propagation velocity of the rim, it can be concluded that the rim is not propelled by gravitational or surface tension forces. There must therefore be a different propulsion mechanism for the rim.

4.3. *PIV experiments: Do entrance vortices cause the rim to form and propagate?*

Since the rim does not propagate like a surface wave, could the vortex, located at the entrance of the tube, drive it as was proposed by Lorenceau *et al.* (2002)? As the column starts to rise, the entrance vortex could deflect the fluid above it outwards, towards the wall of the tube, forming a rim. This effect would weaken as the surface moves away from the entrance vortex, causing the rim to move inward. To investigate this possible effect high-speed particle image velocimetry (PIV) is used.

To perform the PIV measurements, the fluid is seeded with small Dantec Dynamics polyamid tracer particles of radius 25 μm and density 1030 kg m^{-3} that will follow the flow. A laser sheet is shone through the fluid and creates an illuminated plane inside the flow (see figure 1*b*). The light scattered by the tracer particles is captured by a high-speed camera at a frame rate of 1000 frames per second and a resolution of 1280×512 pixels. This series of images is then correlated by multipass algorithms, using DaVis PIV software by LaVision, in order to determine the flow field in the liquid over a two-dimensional area for extended periods of time. The correlation was performed in three passes at sub-pixel accuracy, using 64×64 pixels, 32×32 pixels and 16×16 pixels interrogation windows. The windows overlap by 50%, resulting in one velocity vector every 8×8 pixels.

For the illumination of the high-speed PIV measurements we use a Spectra Physics Stabilite 2017 Argon Ion laser, which outputs continuously at a wavelength of 514.5 nm. Using this continuous laser, the frame rate of the recording camera determines the number of field measurements per second. Power output is an important consideration, because short exposure times are preferable to prevent motion blurring of the particle images. Using the laser at its full 6 W power output allowed an exposure time of 0.1 ms. With a typical flow velocity of $1\,\mathrm{m\,s^{-1}}$ and an image scaling of $10\,\mathrm{pixels\,mm^{-1}}$ the particle images will not move more than one pixel during the exposure, so the blurring effect is minimal. The laser beam is converted into a light sheet by means of three cylindrical lenses. In the experimental setup, the light sheet is oriented vertically, in order to illuminate the flow from below (see figure 1*b*). We found this preferable to a horizontally oriented light sheet shining through the side of the tube, because a horizontally aligned light sheet is reflected many times inside the tube, causing a bright glare near the sides. Moreover, the main flow direction is oriented vertically, so a horizontally oriented light sheet would have to be of considerable width ($\sim 100\,\mathrm{mm}$) to fully illuminate the area of interest.

From these high-speed PIV measurements one obtains typical images of the velocity field such as in figure 8. In this figure the image of the original high-speed recording is overlaid with the obtained PIV results. The PIV software also produces velocity vectors at the free surface and even inside the jet, but these vectors are highly inaccurate, owing to the large optical distortions caused by the curvature of the air/water interface and are thus not shown.

A vortex is visible at the entrance of the tube in figure 8(*a*) and enlarged in figure 8(*b*). The velocity gradients in the interior of this vortex are large†, but can be resolved by our experimental setup. There is however no need to do so, because only the edges of the vortex and not its internal structure are of interest, since this is a measure of whether the vortex is close enough to the free surface to produce the rim. The size of the recirculation zone is indicated by the dashed white line which is the streamline originating at the inner edge of the tube. During the rise of the water column, the entrance vortex stretches in the radial r and the axial z directions. However at the beginning, when the water column starts to rise and the rim is formed, the vortex is still absent. Later, as the vortex is fully developed as in figure 8, it lags considerably behind the column height.

Figure 9 shows the vortex growth from a different perspective. Here the radial flow velocity component v_r at a distance Δz below the rising interface is plotted as a colour plot. The position at which the profiles are monitored is moving upward with the free surface at a fixed distance $\Delta z = 4\,\mathrm{mm}$. The blue colours represent negative v_r (directed towards the $r = 0$ axis). We observe a strong inward-directed radial flow

---

† A closer investigation of the vortex by PIV revealed velocity gradients $\Delta v/\Delta x$ as large as $6 \times 10^2\ \mathrm{s^{-1}}$.

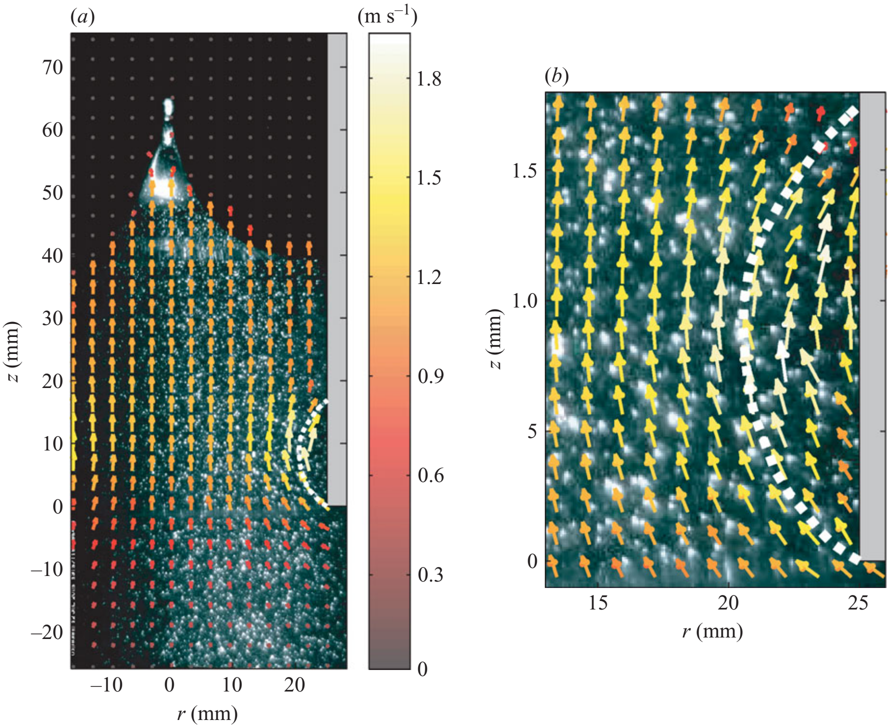

FIGURE 8. The velocity field obtained by PIV overlaid on the original high-speed recording. For clarity, only one-sixteenth of the measured vectors are shown in (*a*) and one-fourth in the enlargement of the vortex region in (*b*). The recording is taken 50 ms after the pressure release and at the time that the water column has reached a height of about 40 mm and the jet has just erupted. The experimental conditions are $H = 150$, $L \gg R$, and $h = 0$ mm. The shaded area on the right depicts the tube wall and the recirculation zone is indicated by the streamline originating at the inner edge of the wall (dashed white line).

near the white line, which indicates the radial position of the rim, assuming a constant velocity of closure. The white dot indicates the moment of jet eruption. The radial flow near the closing rim originates at the tube's bottom edge and spreads into and up the tube over time. The rim seems to be 'pushed along' by this inward flow directly beneath it. The rim propagation can therefore not be described purely as a travelling cylindrical wave; bulk flow effects dictate its movement.

A second observation is that the region of outward-directed flow is far away from the rim and only develops after the rim has passed. The rim therefore cannot be formed by the deflection of fluid towards the tube wall by the entrance vortex as hypothesized and dismissed before. It turns out that the vortex does not play any significant role in the creation or propagation of the rim.

4.4. *The origin of the rim*

In the previous three subsections we have seen that the rim cannot be explained by the initial curvature of the meniscus, nor by a capillary or gravitational surface wave, nor by the vortex at the entrance of the tube. So what can explain the rim formation? To answer this question we look at the development of the flow at the tube entrance in the initial instants of the column rise, since this is where the radial flow 'pushing' the rim seemed to originate.

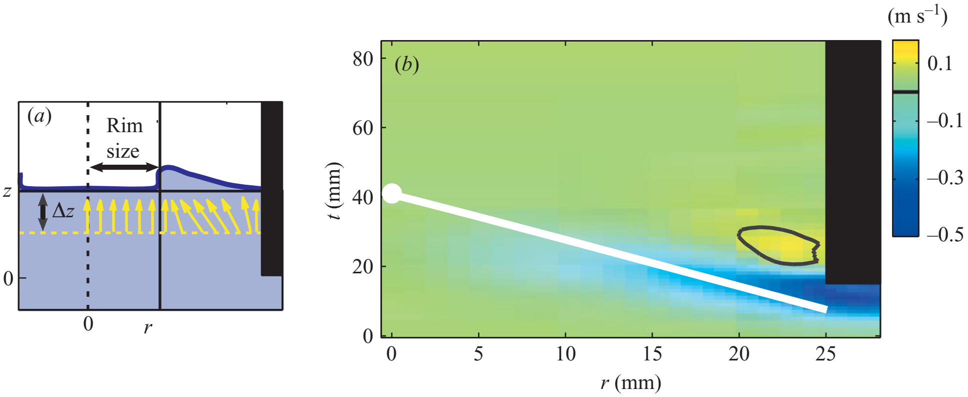

FIGURE 9. (a) A schematic showing how the position at which the flow velocity is monitored in (b) is moving upward with the free surface at a fixed distance Δz. (b) The radial flow velocity component v_r at a distance $\Delta z = 4$ mm below the rising interface, plotted as a colour plot. The blue colours represent negative v_r (directed towards the $r = 0$ axis). We observe a strong inward-directed radial flow near the white line which indicates the time evolution of the radial position of the rim. The white dot indicates the moment of jet eruption. The radial flow near the closing rim originates at the tube's bottom edge and spreads into and up the tube over time. The rim seems to be 'pushed along' by this focusing flow directly beneath it. The focused flow vanishes at the centre of the tube at $r = 0$ mm. The region of outward-directed flow, whose boundary is indicated by the black solid curve of $v_r = 0$, does not influence the rim closure as, at any time t, it is positioned far away from the closing rim. $R = 25$ mm, $L \gg R$, $H = 150$ mm, and $h = 0$ mm.

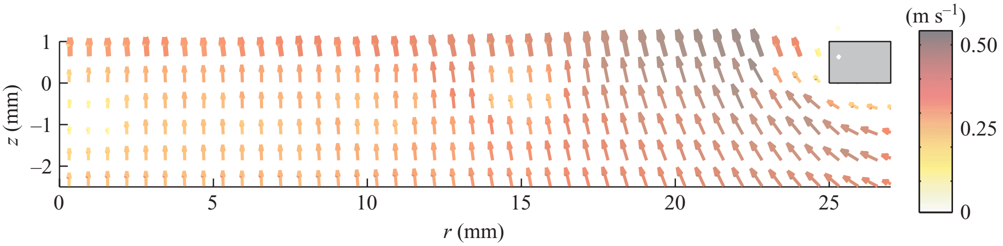

FIGURE 10. The velocity field obtained from PIV measurements at the tube entrance for $H = 150$ mm, 10 ms after the pressure release. The grey shaded area on the right indicates the location of the tube wall. $R = 25$ mm, $L \gg R$, and $h = 0$ mm.

Figure 10 shows the flow in the experiment at the tube entrance 10 ms after the pressure release. The data represent an average of four separate PIV experiments. It is clear that there is a stronger inflow of fluid near $r = R$ on the time scale for the creation of the rim. For this depth H of 150 mm the time scale on which the rim fully develops and starts to move radially inward is 10 ms. The distance of the free surface from the entrance of the tube at that time is only 2 mm. The enhanced axial flow will thus influence the shape of the free surface and produce the rim.

We call this purely geometrical effect of the tube wall forcing the axial and radial flow into the tube and necessarily speeding it up in the process *the funnelling effect*. This enhancement of flow along the inner edge of the tube might at first seem somewhat counter–intuitive. But even in a simplified configuration with a stationary, purely radial inflow into the tube region, such an enhancement arises naturally, as will be show in § 4.5.

4.5. *The funnelling effect*

To corroborate that the funnelling effect is generic to the geometry of a flow entering a contraction, we have performed a potential flow analysis of a simplified configuration with a stationary and constant radial flow at the tube entrance. As stated in the introduction, the Reynolds number is considerable and the funnelling effect develops rapidly compared to the time scale for the development of vorticity, so to a good approximation, the initial flow can be described by potential theory. The flow configuration in this example has been chosen such that it is analytically tractable and does not particularly favour the development of an enhanced axial flow along the outer boundary. In fact, the inflow in the experiment may more resemble a sink flow with a finite size effect with a relatively high radial velocity just below the bottom of the tube, and thus only reinforce the funnelling effect in comparison to the initial condition taken in this example. The full boundary integral simulations of the flow presented in § 6 will yield a much more precise description of the flow within the framework of potential theory.

In the current example we use a constant, purely radial inflow boundary condition in the region directly below the inner tube wall, and a zero normal flow at the bottom of the container, which is positioned at a depth R below the tube (see figure 11*a*). With these boundary conditions, the potential of the flow φ can be solved analytically as detailed in Appendix B, leading to the flow potential and velocity field plotted in figure 11(*b*), where we observe a clear enhancement of the axial flow at the tube wall. This becomes even more clear-cut when looking at the radial and axial velocity components at the tube entrance as a function of r which are shown in figures 11(*c*) and 11(*d*) respectively: the radial component decreases in magnitude as it comes closer to the symmetry-axis of the tube at $r = 0$, directly above the stagnation point located at the bottom of the container, and most importantly, the axial component in this unfavourable example is more than twice as large at the tube wall as in the centre of the tube.

It is this enhanced axial velocity at the tube edge, combined with the considerable radial velocity at this position, that produces the funnelling effect: the enhanced axial flow at the tube edge locally lifts up the free surface and the radial flow component then pushes it inwards, thus creating the rim. So, even for this simplified example of a purely radially driven flow the funnelling effect arises naturally.

5. Investigating the role of the radial flow

In the previous Section we discussed the importance of the radial inflow into the tube for the existence of the funnelling effect and the formation of the rim and jet. In this section we will investigate this in more detail, first by looking at the relative flow into the jet region by subtracting the column velocity, and secondly by experimentally influencing the relative importance of the radial flow component with respect to the axial flow component.

The first idea is inspired by the following. Owing to symmetry the radial component of the flow directly underneath the free surface must vanish at $r = 0$. It is conceivable that due to continuity this vanishing inward radial flow gives rise to a non-zero axial flow into the jet on top of the main axial flow component v_{column}. This induced (extra) axial flow would then locally push the interface up and feed the jet.

To visualize this effect, the column velocity v_{column} is subtracted from the results obtained by the PIV measurements. Figure 12 shows this motion of the fluid relative to the bulk column motion at various times. From figure 12 it is seen that after the

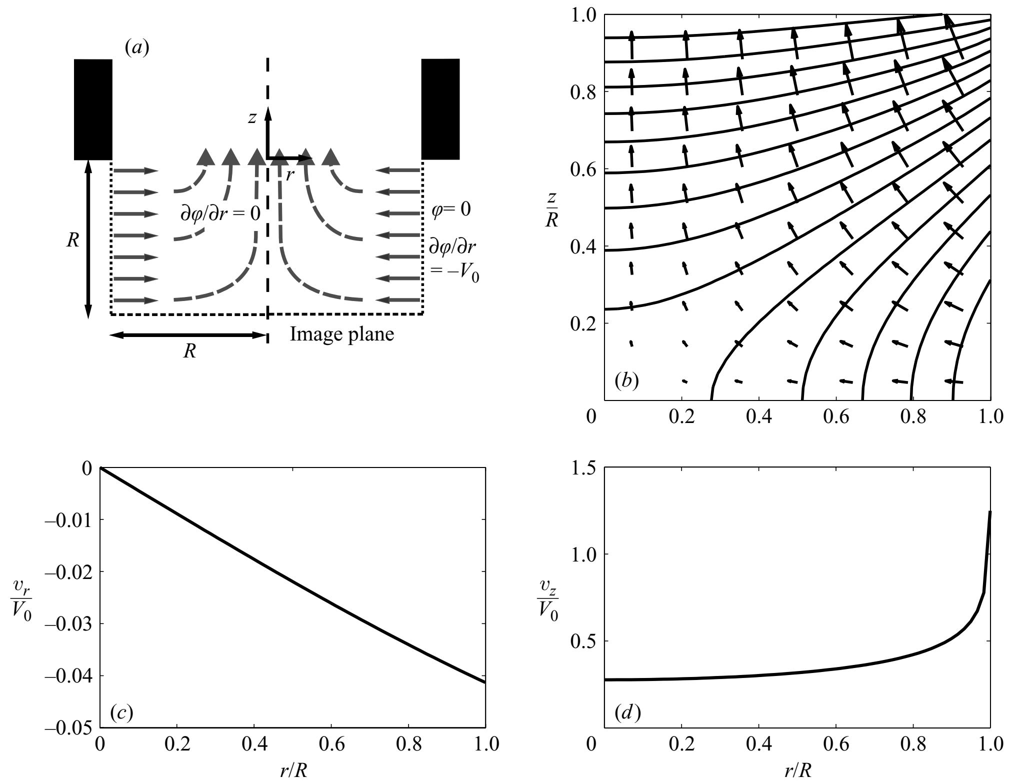

FIGURE 11. (*a*) The initial conditions for the flow potential φ, which illustrates the enhancement of the axial flow along the wall of a contraction. These boundary conditions assume a constant radial inflow of strength V_0 to a depth R below the tube (solid arrows). The expected flow is drawn as dashed arrows. (*b*) The potential and flow given by the configuration of (*a*). As detailed in Appendix B, the potential φ is obtained by (B 3) and is indicated by the isolines. The flow direction and strength obtained by (B 4) and (B 5) are given by the arrows. (*c*, *d*) The radial and axial flow components, v_r and v_z respectively, at the entrance of the tube ($z = R$) obtained by (B 4) and (B 5) for the flow configuration of (*a*). Note that the axial flow is enhanced along the wall.

formation of the rim at $t > 30$ ms the axial component of the flow is increased around $r = 0$ and the interface is pushed upwards in the centre of the tube. The bump which we saw in figures 4 and 7 is thus not just due to the increasing amplitude of the inward-travelling cylindrical wave; there is also an effect of the radial flow beneath it. We also see that there is a continuous flow of fluid from the bulk into the jet. This flow is strongest before the eruption of the jet when we see the rising bump on the interface.

Secondly in this Section we experimentally determine the influence of this effect. To this end we devised a method to enhance and reduce the relative importance of the radial flow in the experiment (figure 13*a*). Reduced radial inflow is obtained by placing a second, larger tube around the first, thus locally blocking the flow in the radial direction directly below the tube inlet (figure 13*b*). Enhanced radial inflow is achieved by simply positioning the tube very close to the bottom, such that the axial inflow is obstructed (figure 13*c*). Both are discussed in more detail below.

Reduced radial inflow. By placing a second, larger tube around the entrance of the main tube, the radial inflow into the tube is reduced (see figure 13*b*). The second tube

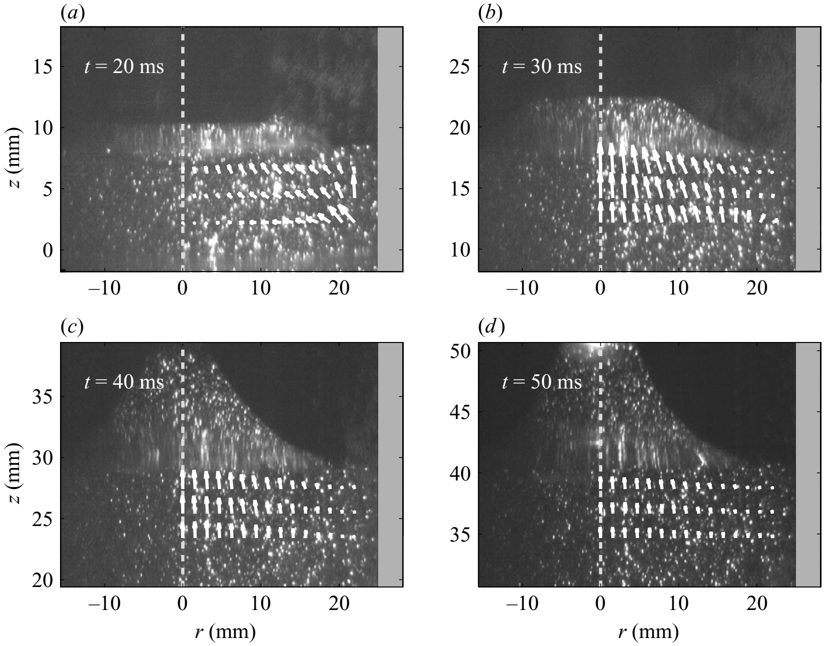

FIGURE 12. The bulk flow inside the tube. The grey shaded area on the right is the tube wall. v_{column} has been subtracted from the velocity data obtained by PIV, therefore the white vectors indicate the flow relative to the column velocity, the velocity with which the free surface rises at the tube wall. The largest vector in (*b*) has a magnitude of $0.3\,\mathrm{m\,s^{-1}}$; the other vectors are scaled linearly. Only the vectors in the region of interest (up to 5 mm below the free surface) are shown. The vectors in the tubular jet are omitted, because imaging through the curved free surfaces of both the tube and the jet causes distortions which make the PIV measurements inaccurate. $R = 25\,\mathrm{mm}$, $L \gg R$, $H = 150\,\mathrm{mm}$, and $h = 0\,\mathrm{mm}$.

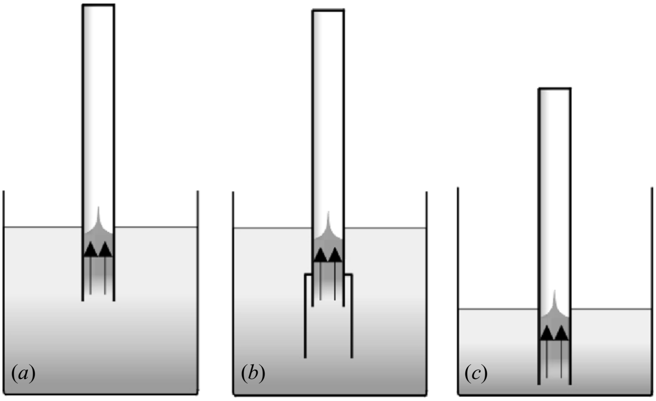

FIGURE 13. The three different flow situations: (*a*) normal flow, (*b*) reduced radial flow, and (*c*) enhanced radial flow.

(inner radius of $R_s = 35\,\mathrm{mm}$) extends twice its radius below the main tube's entrance in order for its entrance effects (e.g. entrance vortex) not to influence the flow into the main tube. Since the liquid still starts with a meniscus in the main tube and the fluid is flowing through a contraction at the main tube's entrance, there will still be a certain amount of radial inflow, though strongly reduced with respect to the 'normal' situation. This situation is similar to the case of $h \gg 0$ if $R_s \approx R$, for which we have already observed that neither a jet nor a rim is formed.

Enhanced radial inflow. Now the tube entrance is placed very near to the bottom of the tank, thereby relatively enhancing the effect of the radial inflow by blocking the inflow in the axial direction (figure 13*c*). Since the entrance depth z_0 is of order R, we must take $L < R$ to significantly increase the radial flow component.

The precise value of L suitable for this setup can be determined by experimentally investigating the influence of L on the rise velocity of the water level v_{column} and the initial jet velocity v_{jet}. From the high-speed camera recordings we observe that the jet velocity is indeed significantly affected by decreasing L below R. While the initial jet velocity increases, the column velocity decreases for small L. When L is decreased below $L = \frac{1}{5}R$ the rising water column detaches from the inside of the tube. Even though this detachment is generally seen for $h < 0$, for such small values of L at $h = 0$ the enhanced radial flow no longer follows the inner corner at the tube's entrance. This phenomenon would make quantification and comparison with other experiments difficult. Therefore $L = \frac{2}{5}R$ (10 mm) was chosen as a suitable value for the radially enhanced flow experiments, since its effect on the initial jet speed is still considerable and detachment of the water column did not occur.

We will first discuss how the radial flow influences the rim, after which the influence on the jet itself will be discussed. In the experiments the strength of the radial inflow influences the shape of the cavity. The cavity is deeper and the rim is steeper for the radially enhanced flow, whereas the cavity is much less prevalent (though not completely absent) in the case of the radially reduced flow (see figure 14). This is also reflected in the flow field at the entrance of the tube. A strong funnelling effect, like that previously observed in figure 10, can be seen to occur in the radially enhanced experiment. In the case of the radial reduced flow this effect seems to be, just like the rim, largely absent.

The propagation mechanism for the rim, the fluid flow directly underneath the free surface, also exhibits a strong dependence on the radial flow component. In the case of radially enhanced flow the v_r component pushing the rim along is stronger compared to the normal flow situation (figure 9). In the case of radial obstructed flow however, this mechanism is observed to be considerably weakened. As a result, the rim propagates at a slower velocity and closes much later than it does for the normal and enhanced radial flow experiments, e.g. at a depth H of 175 mm the time of jet eruption increases from 36 ms to 57 ms (see figure 14).

These experiments underline our earlier observations about the rim, namely that it is created by the funnelling effect at the entrance of the tube and that it is being pushed along by the inward radial flow directly underneath the interface. Both effects are made stronger by enhancing the radial flow component in the entrance flow.

Turning now to the jet creation, we find that the radially obstructed flow produces much weaker jets. Owing to the slower rim collapse the jet also erupts later when compared to the normal and radially enhanced case. The jets produced by the radially enhanced flow are comparable in height to the normal case, even though the total flow of liquid into the tube is restricted (the water column rises considerably slower).

In figure 15(*a*) the ratio of the measured rise velocity v_{column} and the expected rise velocity $\sqrt{gH}$ is plotted against the immersion depth H/R of the column. It is seen that the expected rise velocity is only reached for the considerable depth of $H > 10R$ in the case of the normal flow configuration. The column rise velocity in the two altered setups is found to be much smaller than in the unaltered case. For a better comparison of the initial jet speed in the three different flow configurations, in figure 15(*b*)

Normal inflow

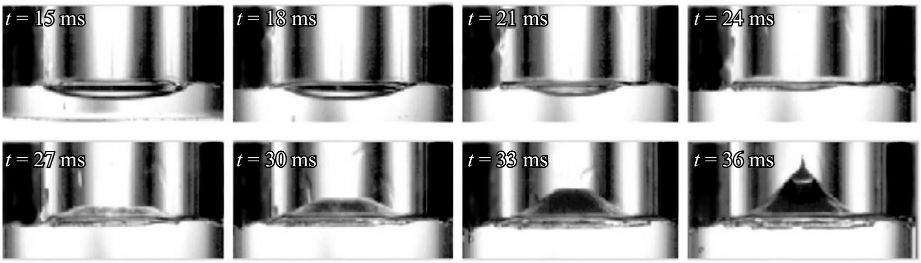

Radially reduced inflow

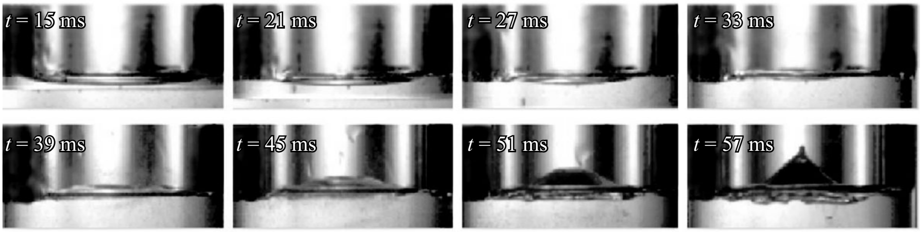

Radially enhanced inflow

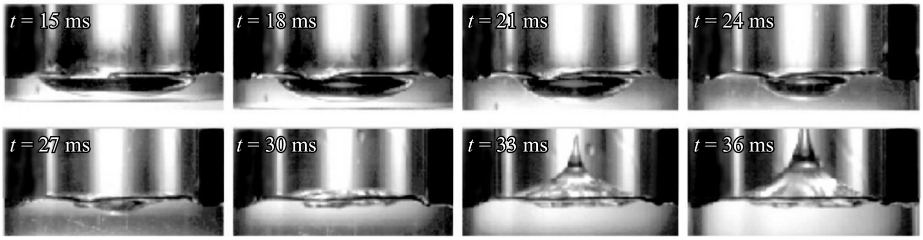

FIGURE 14. Close-up view of the closing rim for normal (top), radially reduced (middle), and radially enhanced (bottom) flow (see main text for the details of the geometry). Clearly, the rim is much more pronounced for stronger radial flows. The time interval between consecutive images is $\Delta t = 3$ ms for the top and bottom series, and twice this value ($\Delta t = 6$ ms) for the middle series, owing to the slower propagation speed of the rim in this case. In each case, the first image of each series is taken at $t = 15$ ms from the pressure release time. $R = 25\,\mathrm{mm}$, $L \gg R$, $H = 175\,\mathrm{mm}$, and $h = 0\,\mathrm{mm}$.

we therefore normalize the initial jet velocities by the measured v_{column} instead of by using $\sqrt{gH}$. The radially enhanced setup consistently produces the strongest jets, even though the total fluid flux into the tube is restricted. The radially obstructed setup on the other hand produces the weakest jets. The normalized initial jet velocities seem to level off for $H > 10R$ (250 mm) and scale with v_{column} in this limit.

We conclude that the increase of the radial flow strongly enhances the erupting jet. The enhanced radial flow setup has a stronger radial flow and collapse, and subsequently, a stronger axial flow feeding the jet after the rim collapse. This is all in good agreement with the mechanism of rim and jet formation outlined in the previous Section.

In addition, the findings of this Section also shed light on the mechanism by which the initial meniscus height h determines the strength of the jet (see figures 2 and 3). For $h > 0$, with the initial meniscus well inside the tube, the local radial inflow at the free surface is effectively blocked by the tube walls, preventing the formation of the

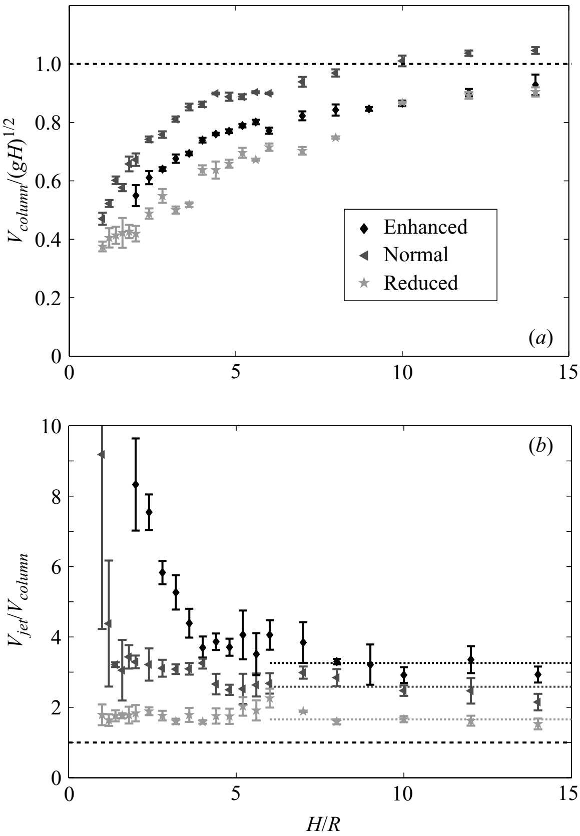

FIGURE 15. The influence of the radial flow on the initial jet and column velocities (see figure 13). The radially reduced flow configuration (light grey stars) and the radially enhanced flow configuration (black diamonds) are compared to the normal flow situation (dark grey triangles). (*a*) The column velocity as a function of the depth. Only for large depth H does v_{column} tend to $\sqrt{gH}$. (*b*) The initial jet velocity v_{jet} normalized by the column velocity v_{column} as a function of the depth. As the radial flow is enhanced, the initial jet velocity is found to be considerably larger than v_{column}. For large depth H the ratio v_{jet}/v_{column} tends to a constant. $R = 25\,\mathrm{mm}$, $L \gg R$, and $h = 0\,\mathrm{mm}$.

rim and therefore producing a small jet at most. By contrast, for $h < 0$ the meniscus bulges out of the tube and there will be a strong local radial inflow at the free surface, resulting in a massive rim and a strong jet.

6. Comparison between boundary integral simulations and experiments

To further support our findings and corroborate that vorticity indeed plays no significant role in the creation of the tubular jet, we have performed a potential flow calculation. In this, the exact geometry of the problem is taken into account, including the initial shape of the meniscus and the moving free surface, making it necessary to solve the potential numerically by means of a boundary integral simulation (Pozrikidis 1997) which is discussed in more detail in Appendix C.

We start from a numerical initial condition obtained from the Young–Laplace equation which very nicely corresponds to the experimentally observed shape of the meniscus (see Appendix C.1 for details) and then calculate the evolution of the free

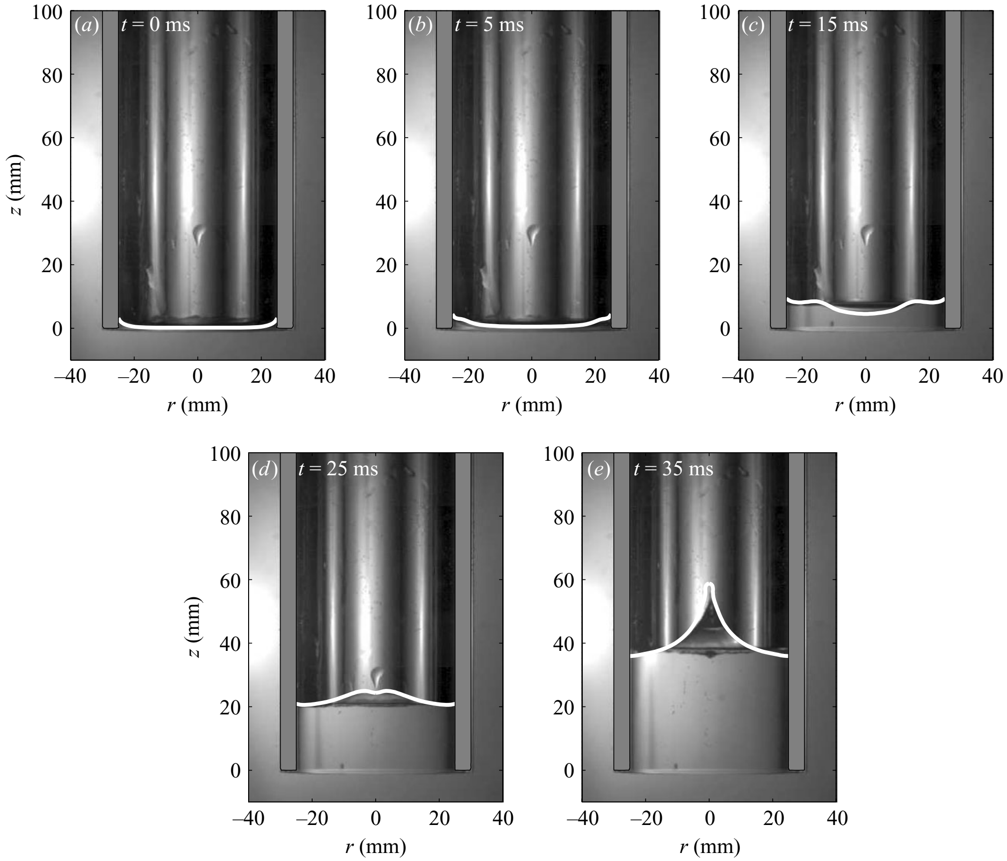

FIGURE 16. The experiments (snapshots) overlaid by the numerical result (white line) for the free surface at different instances in time. The tube wall used for the numerical calculation is indicated by the grey shaded area. The height of the numerically obtained free surface is adjusted to compensate for the faster rising of the liquid column in our numerical calculations. The shape and time evolution of the numerically obtained free surface is shown without any further adjustment. $R = 25\,\text{mm}$, $L \gg R$, $H = 300\,\text{mm}$, and $h = 0\,\text{mm}$.

surface in time. When we compare the boundary integral simulation to an experiment under the same conditions, the first striking observation is the excellent agreement of the shape of the free surface, the velocity of the rim, and the moment at which the jet erupts (see figure 16). However, we find the water column to rise more quickly in the numerical calculations compared to the experiments. In both cases the rise velocities v_{column} tend to the same constant velocity, but the initial acceleration of the water column in the numerical calculations is considerably higher. This difference in acceleration could be due to a difference in the global flow structure, since in the numerical calculations only the bottom wall of the tank is taken into consideration and its sidewalls are neglected. These sidewalls could only be included in the calculations by introducing them as image planes, and subsequently introducing four more tubes into the numerical calculations, but this would call for a full three–dimensional calculation which is unachievable for our axisymmetric boundary integral code. The tubular jet, however, depends only on the local flow structure, namely the funnelling effect at the tube entrance and continuity at the centre of the tube, which allows us to simply compensate for the increased rising of the water column as was done in figure 16, giving excellent agreement between simulation and experiment.

Most notably, in the numerical calculations we observe the same funnelling effect along the edge of the tube generating the cavity as in experiment, which is clearly visible in figures 16(*b*) and 16(*c*). The propulsion of the rim by the radial flow is also observed, including the rising of the centre bump and the eruption of the jet at exactly the same time as in the experiment (figure 16*d*, *e*).

Since this potential flow calculation does not include viscosity and vorticity, we again conclude that vorticity is not part of any of the mechanisms leading to the eruption of the tubular jet.

7. Conclusions

We have investigated the origins of the tubular jet and found that the inward radial flow strongly influences the strength and formation of the jet. Several effects, all originating from the converging radial inflow, work together to create the tubular jet. The results of high-speed imaging, PIV measurements, and simulations lead to the following sequence of events:

Directly after the pressure in the tube is released, liquid is funnelled into the tube. If the meniscus is close enough to the bottom of the tube, the axial component of the flow pushes the perimeter of the interface upwards forming a rim.

This rim, propagating more like a hydraulic jump or bore than a surface wave, travels inward and is pushed along by the inward radial flow directly underneath the interface. The singularity that occurs when the rim reaches the centre is manifested as a sharp jet shooting upwards.

During the formation and propagation of the rim, a bump of fluid forms on the surface of the rising water column. We have shown through PIV experiments that this bump is not merely the increase in amplitude that is seen in converging cylindrical waves. Fluid flows up into the bump from below, driven by the converging flow in the bulk of the column. This flow continues to feed the singularity caused by the rim for a short time. Lorenceau *et al.* (2002) dismissed the idea that the tubular jet is caused by flow convergence on the grounds that such an effect would not appear after a delay. We have shown in experiments and irrotational potential flow simulations that the flow convergence affects the flow not after a delay, but from the very beginning of the process.

By experimentally obstructing and enhancing the radial flow component, we find that the bump and rim both depend on converging flow for their formation. The two mechanisms evolve separately, and then merge together to create the tubular jet.

Thus we have shown that the origin of the tubular jet lies entirely in the focusing of flow entering the tube. Therefore, the tubular jet is similar to jets that are produced by a geometrical flow focusing of the free surface of the liquid as discussed in the introduction of this paper. There are important differences however. First, it is not the initial shape of the free surface that produces the tubular jet, but the fact that the liquid has to enter the space confined by the tube walls. Secondly, the uniqueness of the tubular jet stems from the merging of two initially separate events: the creation, propagation, and collapse of the rim together with the continuous feeding of the jet by the enhanced vertical flow at the axis of the tube.

We would like to thank Andrea Prosperetti and Mark Stijnman for the development of the Boundary Integral code. We are also grateful to Johanna Bos and Roderick

Knuiman for their experimental input. The work is part of the research program of FOM, which is financially supported by NWO, and R.B. acknowledges financial support.

Appendix A. Gravitational and capillary waves

In figure 7 we observe that the rim overtakes the smaller capillary waves as it travels to the centre. In this Appendix we check whether a gravitational wave of the size of the rim would indeed travel faster than the observed capillary waves.

The surface waves are observed during the initial acceleration of the water column, therefore the waves are subject to an acceleration besides gravity. If we take z_0 to be of order R (Lorenceau *et al.* 2002) and differentiate (2.2), we find an initial column acceleration of $\ddot{z}_{column} = (H/R)g$. If we introduce the total acceleration $g(1+H/R)$ into the dispersion relation of a surface wave in the deep water approximation (Landau & Lifshitz 1987), we find

$$c(k) = \frac{\omega}{k} = \sqrt{\frac{g}{k}\left(1+\frac{H}{R}\right)+\frac{\sigma k}{\rho}}, \tag{A 1}$$

with k being the wavenumber and ρ the density of the liquid. However, if the rim shape is a surface wave, it cannot be described by a simple monochromatic wave; it should be a superposition of many waves of varying wavenumber. Its propagation speed is thus given by the group velocity c_g, defined as the derivative of the temporal frequency with respect to the spatial frequency,

$$c_g(k) = \frac{\mathrm{d}\omega}{\mathrm{d}k} = c(k) + \frac{-g/k(1+H/R)+\sigma k/\rho}{2c(k)}. \tag{A 2}$$

From (A 2) we find that the smaller, inner waves of $2\pi/k = 3\,\mathrm{mm}$ will have a typical velocity of order $0.6\,\mathrm{m\,s^{-1}}$, while a surface wave of the size of the rim (roughly $2\pi/k =$ 1 cm or larger) would travel much slower, namely at a speed of $0.3\ \mathrm{m\,s^{-1}}$ for the depth of figure 7 ($H = 200\,\mathrm{mm}$). Since the rim shape is seen to ‘overtake’ the capillary waves in figure 7, it thus cannot be a gravitational surface wave and must be propelled by the liquid flowing in the tube.

Although (A 1) is commonly found in the context of two-dimensional waves, it can be shown (see e.g. Saylor, Szeri & Foulks 2000) that the dispersion relation also holds for axisymmetric waves in the capillary regime.

Appendix B. Calculation of the funnelling effect

In this Appendix we calculate the flow potential in the region below the tube in the simplified configuration with a stationary and constant radial inflow at the tube entrance, which is discussed in § 4.5. For short time scales this leads to a potential flow problem in which gravity can be neglected and the boundary conditions are given by (see figure 11*a*)

$$\left(\frac{\partial\varphi}{\partial r}\right)_{r=R} = -V_0\ , \qquad \left(\frac{\partial\varphi}{\partial z}\right)_{z=0} = 0, \tag{B 1}$$

of which the latter can be taken care of by the image method: creating an image of the flow configuration in the plane $z = 0$ will create the correct boundary condition at the bottom.

The axisymmetric form of Green's identity can be employed to write the solution to the Laplace equation $\nabla^2\varphi = 0$ for the flow potential $\varphi(r, z)$ in terms of an integral over the boundary S of the domain (Pozrikidis 1997), namely

$$\varphi = \frac{1}{2}\int_S \hat{r}\left(G\frac{\partial\varphi}{\partial \boldsymbol{n}} - \varphi\frac{\partial G}{\partial \boldsymbol{n}}\right)\mathrm{d}S, \tag{B 2}$$

where $\boldsymbol{n}$ is the normal to the surface S, and

$$G = \frac{2}{\pi}\int_0^{\pi/2}((r+\hat{r})^2 + (z-\hat{z})^2 - 4r\hat{r}\cos^2\theta)^{-1/2}\mathrm{d}\theta.$$

In this way, integrating over all points $(\hat{r}, \hat{z})$ on the boundary S, the potential φ at any point (r, z) in the bulk can be obtained.

If we now use the boundary conditions discussed above and depicted in figure 11(*a*), we can rewrite (B 2) as

$$\varphi = -\frac{V_0 R}{\pi}\int_{-L}^{L}\int_0^{\pi/2} a^{-1/2}\,\mathrm{d}\theta\,\mathrm{d}\hat{z}, \tag{B 3}$$

with

$$a = (r+R)^2 + (z-\hat{z})^2 - 4rR\cos^2\theta.$$

Carrying out the integration of (B 3) with respect to $\hat{z}$ and θ, and subsequently differentiating with respect to either r or z, yields the radial v_r and axial v_z flow velocities at point (r, z), namely

$$v_r = \frac{\partial\varphi}{\partial r} = -\frac{V_0}{\pi}\left[G(r,z) + G(r,-z)\right], \tag{B 4}$$

with

$$G(r,z) = R\,\frac{z-L}{2r\sqrt{b}}\left[\frac{r-R}{r+R}\,\Pi\left(\frac{4rR}{(r+R)^2}, \sqrt{\frac{4rR}{b}}\right) + K\left(\sqrt{\frac{4rR}{b}}\right)\right],$$

and

$$v_z = \frac{\partial\varphi}{\partial z} = \frac{V_0}{\pi}[F(r,z) - F(r,-z)], \tag{B 5}$$

with

$$F(r,z) = \frac{R}{\sqrt{b}}\,K\left(\sqrt{\frac{4rR}{b}}\right).$$

Here $\Pi(n,k) = \int_0^{\pi/2}((1-n\cos^2\theta)\sqrt{1-k^2\cos^2\theta})^{-1}\mathrm{d}\theta$ is the complete elliptic integral of the third kind, $K(k) = \int_0^{\pi/2}(\sqrt{1-k^2\cos^2\theta})^{-1}\mathrm{d}\theta$ is the complete elliptic integral of the first kind, and $b = (r+R)^2 + (z-L)^2$.

The flow potential and flow field equations (B 3), (B 4), and (B 5) are plotted in figures 11(*b*), 11(*c*), and 11(*d*).

Appendix C. Boundary integral simulation

To verify that vorticity plays no role in the creation of the tubular jet, we performed axisymmetric boundary integral simulations (Pozrikidis 1997). Since the exact geometry of the problem is now taken into account, including the moving free surface, the potential flow formulation briefly discussed in Appendix B is now solved

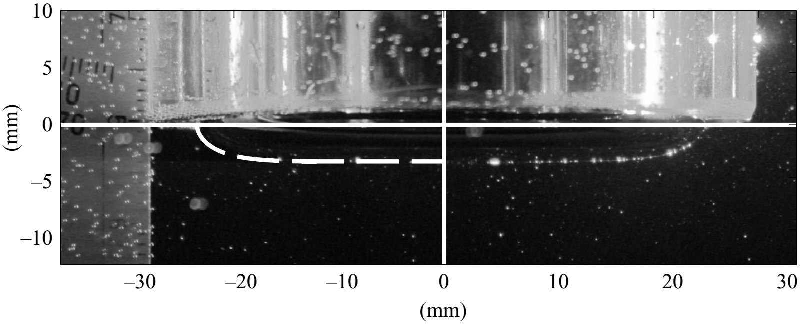

FIGURE 17. Comparison of the meniscus obtained by the shooting routine with the meniscus observed in the experiment. The numerical solution (dashed white line) is overlaid on the left half of a photograph of the meniscus ($h = -3.5$ mm, $R = 25$ mm). The interface in the photograph is illuminated by a laser sheet and can be seen in the right half.

numerically. In § 3 we found that the initial state of the system, namely the meniscus, has a profound effect on the tubular jet. So, as a prerequisite for obtaining realistic simulation results we first have to accurately capture this initial condition.

C.1. *Initial condition for the boundary integral simulation*

In order to obtain the shape of the meniscus as an initial condition for the simulations, we use the Young–Laplace equation (Middleman 1995) to describe the shape of the liquid–gas interface in equilibrium,

$$P_{water} - P_{air} = 2\sigma\kappa, \tag{C 1}$$

where P_{water} and P_{air} are the pressures at the air–water interface, σ is the surface tension, and κ is the mean curvature of the interface. The hydrostatic pressure in the water is defined as $P_{water} = \rho g(H - z)$ and as long as the surface is flat at $r = 0$ (this is the case for R sufficiently larger than the capillary length), the air pressure inside the tube is given by $P_{air} = \rho g(H - h)$. The air–water interface is represented as an axisymmetric surface described by a revolution of the curve $r(z)$. This curve has endpoints at $[0, R]$ at the inner wall of the tube and $[h, 0]$ on the z-axis. The mean curvature at any point (r, z) on such a surface is given by

$$2\kappa = \frac{\mathrm{d}^2 r/\mathrm{d}z^2}{[1 + (\mathrm{d}r/\mathrm{d}z)^2]^{3/2}} + \frac{1}{r[1 + (\mathrm{d}r/\mathrm{d}z)^2]^{1/2}}. \tag{C 2}$$

Combining (C 1) and (C 2) we can obtain an ODE which must be solved numerically using a shooting method, because the two boundary conditions are defined at two different ends:

1. $r(0) = R$; the interface must meet the tube's inner edge,
2. $r(h) = 0$; the meniscus depth is h.

In this way a meniscus shape is obtained which is in excellent agreement with the experimentally observed meniscus shape, as can be seen in figure 17. This numerical meniscus shape will be used as the initial condition in our boundary integral simulations.

C.2. *Boundary integral simulation*

The moving free surface is iteratively solved in time using an axisymmetric boundary integral formulation for the potential φ with the standard kinematic and dynamic boundary conditions (Oguz & Prosperetti 1990; Longuet-Higgins *et al.* 1991; Oguz

& Prosperetti 1993; Boulstone & Blake 1993; Blake *et al.* 1997; Gaudet 1998; Zhu, Oguz & Prosperetti 2000; Zhang *et al.* 2001; Prosperetti 2002; Leppinen & Lister 2003; Gordillo *et al.* 2005; Gordillo & Perez-Saborid 2006; Eggers *et al.* 2007).

The kinematic boundary condition on an impermeable surface effectively specifies that there can be no flow across the free surface. This means that the surface must move with the local fluid velocity, perpendicular to the surface $\nabla\varphi \cdot \boldsymbol{n}$. At the static, solid wall of the tube, the boundary condition simply states that there can be no flow across the boundary, so $\nabla\varphi \cdot \boldsymbol{n} = 0$.

At the free surface the normal stresses also need to be continuous. In our case at the other side of the fluid interface, there is a gas with negligible dynamic effects and a constant pressure P_{air}. If we assume that the viscous stress contribution is negligible, then the pressure at the surface has to satisfy (C 1). It can be shown that the contribution of the surface vorticity to the pressure is negligible, thus we can use the unsteady Bernoulli equation to obtain an implicit condition for $\partial\varphi/\partial t$ along the free surface. This condition is often referred to as the dynamic boundary condition.

As an added complication the contact points are not fixed at a particular geometrical location. The contact points are allowed to move freely along the solid walls of the tube, following the local fluid velocity. Note that the contact line, like all of the fluid, does not experience any friction along the wall.

There is however also a numerical difficulty of the boundary integral formulation related to the free surface. When the free surface closes on itself, the free surface curve will self-intersect and cause a singularity. It is possible to set up a procedure to detect imminent self-intersection and perform a pinch-off by cutting off the drop or bubble after reconnecting the free surface. Such a procedure is however not implemented in our simulation. This severe numerical difficulty limits the range of our numerical investigation to figure 16 and prevents a thorough numerical study of the parameters, because as the surface cavity closes and its walls intersect, or droplets are pinched off at the tip of the jet by the Plateau instability, the simulation halts. Nevertheless, the excellent agreement between the simulations and experiment in figure 16 makes clear that the inviscid and vorticity-free description of potential flow suffices to recreate the tubular jet.

REFERENCES

Antkowiak, A., Bremond, N., Le Dizés, S. & Villermaux, E. 2007 Short-term dynamics of a density interface following an impact. *J. Fluid Mech.* **577**, 241–250.

Bergmann, R., van der Meer, D., Stijnman, M., Sandtke, M., Prosperetti, A. & Lohse, D. 2006 Giant bubble pinch-off. *Phys. Rev. Lett.* **96**, 154505–154800.

Birkhoff, G., MacDougall, D., Pugh, E. & Taylor, G. 1948 Explosives with lined cavities. *J. Appl. Phys.* **19** (6), 563–582.

Blake, J. R., Hooton, M. C., Robinson, P. B. & Tong, R. P. 1997 Collapsing cavities, toroidal bubbles and jet impact. *Phil. Trans. R. Soc. Lond.* A **355**, 537–550.

Bohr, T., Dimon, P. & Putkaradze, V. 1993 Shallow-water approach to the circular hydraulic jumps. *J. Fluid Mech.* **254**, 635–648.

Boulstone, J. M. & Blake, J. R. 1993 Gas-bubbles bursting at a free-surface. *J. Fluid Mech.* **254**, 437–466.

Burton, J. C., Waldrep, R. & Taborek, P. 2005 Scaling and instabilities in bubble pinch-off. *Phys. Rev. Lett.* **94**, 184502.

Caballero Robledo, G. A., Bergmann, R., van der Meer, D., Prosperetti, A. & Lohse, D. 2007 Role of air in granular jet formation. *Phys. Rev. Lett.* **99**, 018001.

Chen, A. & Basaran, O. 2002 A new method for significantly reducing drop radius without reducing nozzle radius in drop-on-demand drop production. *Phys. Fluids* **14**, L1.

Ducleaux, V., Caillé, F., Duez, C., Ybert, C., Bocquet, L. & Clanet, C. 2007 Dynamics of transient cavities, *J. Fluid Mech.* **591**, 1–19.

Eggers, J., Fontelos, M. A., Leppinen, D. & Snoeijer, J. H. 2007 Theory of the collapsing axisymmetric cavity. *Phys. Rev. Lett.* **98**, 094502.

Gaudet, S. 1998 Numerical simulation of circular disks entering the free surface of a fluid. *Phys. Fluids* **10**, 2489.

Gordillo, J. M. & Perez-Saborid, M. 2006 Dynamics of bubble-growth and detachment from a needle. *J. Fluid Mech.* **562**, 303.

Gordillo, J. M., Sevilla, A., Rodriguez-Rodriguez, J. & Martinez- Bazan, C. 2005 Axisymmetric bubble pinch-off at high Reynolds numbers. *Phys. Rev. Lett.* **95**, 194501.

de Jong, J., de Bruin, G., Reinten, H., van den Berg, M., Wijshoff, H., Versluis, M. & Lohse, D. 2006*a* Air entrapment in piezo-driven inkjet printheads. *J. Acoust. Soc. Am.* **120**, 1257–1265.

de Jong, J., Jeurissen, R., Borel, H., van den Berg, M., Versluis, M., Wijshoff, H., Prosperetti, A., Reinten, H. & Lohse, D. 2006*b* Entrapped air bubbles in piezo-driven inkjet printing: Their effect on the droplet velocity. *Phys. Fluids* **18**, 121511.

Landau, L. D. & Lifshitz, E. M. 1987 *Fluid Mechanics*. Pergamon.

Le, H. 1998 Progress and trends in ink-jet printing technology. *J. Imag. Sci. Tech* **42**, 49–62.

Leppinen, D. & Lister, J. R. 2003 Capillary pinch-off in inviscid fluids. *Phys. Fluids* **15**, 568.

Liger-Belair, G., Lemaresquier, H., Robillard, B., Duteurtre, B. & Jeandet, P. 2001 The secrets of fizz in champagne wines: A phenomenological study. *Am. J. Enol. Viticult.* **52**, 88–92.

Lohse, D., Bergmann, R., Mikkelsen, R., Zeilstra, C., van der Meer, D., Versluis, M., van der Weele, K., van der Hoef, M. & Kuipers, H. 2004 Impact on soft sand: Void collapse and jet formation. *Phys. Rev. Lett.* **93**, 198003.

Longuet-Higgins, M. S., Kerman, B. R. & Lunde, K. 1991 The release of air bubbles from an underwater nozzle. *J. Fluid Mech.* **230**, 365–390.

Lorenceau, E., Quere, D., Ollitrault, J.-Y. & Clanet, C. 2002 Gravitational oscillations of a liquid column in a tube. *Phys. Fluids* **14**, 1985–1992.

Middleman, S. 1995 *Modeling Axisymmetric Flows*. Academic.

Munson, B., Young, D. & Okiishi, T. H. 1998 *Fundamentals of Fluid Mechanics*. John Wiley & Sons.

Oguz, H. & Prosperetti, A. 1990 Bubble entrainment by the impact of drops on liquid surfaces. *J. Fluid Mech.* **219**, 143–179.

Oguz, H. & Prosperetti, A. 1993 Dynamics of bubble growth and detachment from a needle. *J. Fluid Mech.* **257**, 111–145.

Pozrikidis, C. 1997 *Introduction to Theoretical and Computational Fluid Dynamics*. Oxford University Press.

Prosperetti, A. 2002 *Drop Surface Interactions*. Springer.

Royer, J., Corwin, E., Flior, A., Cordero, M.-L., Rivers, M., Eng, P. & Jaeger, H. 2005 Formation of granular jets observed by high-speed x-ray radiography. *Nat. Phys.* **1**, 164–167.

Saylor, J., Szeri, A. & Foulks, G. 2000 Measurement of surfactant properties using a circular capillary wave field. *Exps. Fluids* **29**, 509–518.

Suryo, R., Doshi, P. & Basaran, O.A. 2004 Non-self-similar, linear dynamics during pinch-off of a hollow annular jet. *Phys. Fluids* **16**, 4177.

Thoroddsen, S. & Shen, A. 2001 Granular jets. *Phys. Fluids* **13**, 4–6.

Worthington, A. 1908 *A Study of Splashes*. London: Longman and Green.

Zeff, B., Kleber, B., Fineberg, J. & Lathrop, D. 2000 Singularity dynamics in curvature collapse and jet eruption on a fluid surface. *Nature* **403**, 401–404.

Zhang, Y. L., Yeo, K. S., Khoo, B. S. & Wang, C. 2001 3D jet impact and toroidal bubbles. *J. Comput. Phys.* **166**, 336–360.

Zhu, Y., Oguz, H. & Prosperetti, A. 2000 On the mechanism of air entrainment by liquid jets at a free surface. *J. Fluid Mech.* **404**, 151–177.